Exploration of chemical probes and conformational flexibility of GID4 - the substrate receptor of human CTLH E3 ligase complex

Daria Kotlarek*, Katarzyna Dudek*, Bartosz Woźniak*, Martyna W. Pastok*, Dmitrii Shishov, Sylvain Cottens, Michał Biśta, Emilia Krzywiecka, Karolina M. Górecka-Minakowska, Kinga Jurczak, Tomas Drmota, Justyna Adamczyk, Szymon Faliński, Daria Gajewska, Marta Klejnot, Aleksandra Król, Monika Cuprych-Belter, Iwona Mames, Arnaud Mathieu, Aleksandra Podkówka, Kamil Przytulski, Alicja N. Skowron, Magdalena Sypień, Toshimitsu Takagi, Weronika Wanat, Igor H. Wierzbicki, Janusz Wiśniewski, Anna Szlachcic, Ziemowit Pokładek, Michał J. Walczak†

Captor Therapeutics Inc., ul. Duńska 11, 54-247 Wrocław, Poland
*Equal contributions
†Corresponding author: michal.walczak@captortherapeutics.com

ABSTRACT

The application of targeted protein degradation (TPD) is currently constrained by the limited availability of low-molecular-weight molecules that can recruit E3 ligases other than CRBN (Cereblon) or VHL (Von Hippel-Lindau ligase). In this study, we present the structure-based drug design (SBDD) of high-affinity ligands that engage E3 ligase GID4 (Glucose-induced degradation protein 4) in biophysical and cellular experiments. Through structural studies and molecular modeling, we identified three groups (clusters) of compounds that induce distinct conformations of GID4. We identified potential exit vectors and used the most promising ligand as a building block to prepare bifunctional degraders in the form of proteolysis-targeting chimeras (PROTACs). Although ternary complex formation was successful *in vitro*, degradation of BRD4 was not observed, highlighting the need for further optimization of the degraders. We also theoretically investigated the likelihood of the identified GID4 conformations participating in protein-protein interactions mediated by molecular glue mechanisms. We believe the expanded ligand diversity

discovered in this study may pave the way for tuning the selectivity and efficacy of protein-protein interactions involving GID4 and its neosubstrates.

GRAPHICAL ABSTRACT

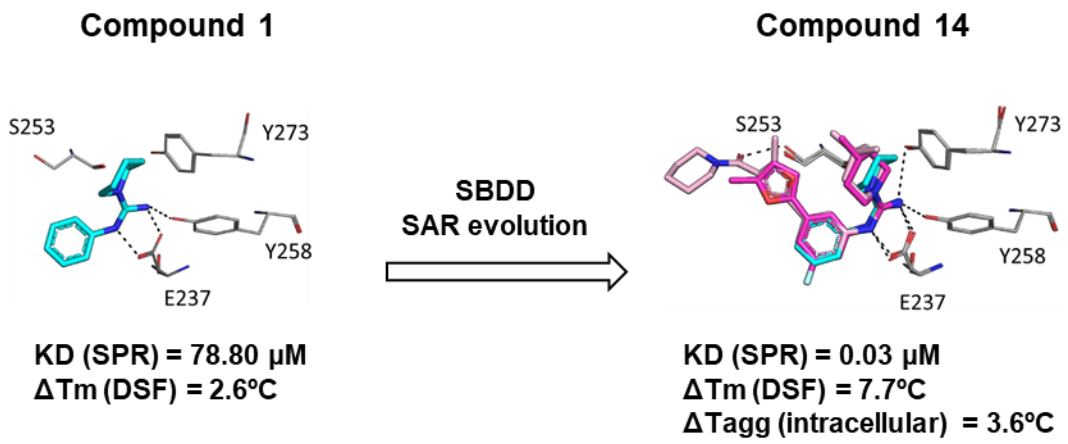

INTRODUCTION

Targeted protein degradation (TPD) is emerging as a new modality in drug discovery and as opposed to protein inhibitors, offers pharmacology of event rather than pharmacology of occupancy. TPD relies on the utilization of the endogenous cell machinery of the ubiquitin-proteasome system (UPS) for the degradation of disease-related proteins. This mechanism is mediated either via molecular glues or modular molecules called proteolysis targeting chimeras (PROTACs). Despite certain differences between these two modalities, they both converge by bringing into proximity the E3 ligase complex and the protein of interest for its subsequent ubiquitination and degradation in the proteasome. TPD offers significant advantages over traditional inhibitor-based approaches. One of them is targeting proteins without well-defined binding pockets, for instance, transcription factors and scaffolding proteins, which until now have been considered “undruggable”. Nonetheless, the substantial obstacle to the rapid progress of the technology is the insufficient number of new, validated E3 ligases, beyond the “workhorses of TPD” employed most often, cereblon (CRBN) and von Hippel-Lindau (VHL) proteins. Therefore, recent efforts in this area aim to extend the diversity of E3 ligases for TPD application drawing from about 600 E3 ligases identified in humans. It is expected that the discovery of chemical handles to engage more E3 ligases will enable targeted protein degradation in a tissue- or disease-

specific manner. In addition, a greater variety of available E3s would be beneficial for combination therapies, reducing side effects, and minimizing acquired resistance.

The C-terminal to LisH (CTLH) complex is an evolutionarily conserved, multi-subunit complex maintaining the E3 ligase activity. Its function is well understood in budding yeast, where it participates in the degradation of the gluconeogenic enzymes once the cell enters glucose-replete conditions (Hämmerle et al. 1998; Regelmann et al. 2003). It was shown that this metabolic switch is dependent on the CTLH substrate receptor Glucose-Induced Degradation protein 4 homolog (GID4) (Santt et al. 2008). This observation paved the way for the determination of the N-terminal proline-containing sequence (Pro/N-end) derived from the enzymes Fbp1, Icl1, and Mdh2 as the recognition motif for GID4 (Chen et al. 2017). The molecular details of GID4/CTLH binding to the Pro/N-end degron were revealed from crystal structures of human GID4 (hGID4) bound to N-terminal peptides (Dong et al. 2018). GID4 adopts an eight-strand β-barrel with a deep cavity. The central tunnel surrounded by four flexible loops (L1-L4) forms a binding site for the N-terminus of a peptide. A few available crystal structures suggest a substantial degree of plasticity within the binding pocket, indicating the possibility of various proteins binding endogenously, making it a challenging target for the development of small molecule binders.

Indeed, the ability to accommodate various types of degron sequences inside the GID4 binding pocket was demonstrated by Dong et al. 2020. A mutation-scanning peptide array and phage display screening revealed the importance of hydrophobic residues at position 1 (either Pro, Ile, Leu, Val, Phe, or Trp), that can be followed by a small side-chain residue at position 2. Most amino acids are accepted at position 3 except for Gly, Asp, and Pro. Later positions allow any amino acid; however, it was shown that the downstream pattern is important for binding and affinity (Dong et al. 2020). The ability to bind various sequences was acknowledged by the pliability of the four hairpin loops (L1-L4), evidenced by the crystal structures of hGID4. These findings might indicate a broader range of GID4 substrates beyond proteins or peptides containing a Pro N-degron motif. The physiological substrates of hGID4 have been recently identified with the help of tools like GID4-specific chemical probe PFI-7 (Yazdi, et al. 2023) and methods such as proximity-dependent biotinylation and degradomics. Notably, the mammalian counterparts of *S. cerevisiae's* Fbp1, Icl1, and Mdh2 proteins miss the Nt-Pro residue and are not targeted by the GID4/CTLH complex. Recently, Yi et al. 2024 found a link between the function of the GID4/CTLH complex in yeasts and humans by demonstrating the degradation of a metabolic enzyme, 3-hydroxy-3-

methylglutaryl (HMG)-coenzyme A (CoA) synthase 1 (HMGCS1). The HMGCS1 is recognized by its Nt-Pro degron motif by the GID4/CTLH upon nutrient stress and mTORC1 inhibition. On the other hand, Bagci et al. 2023 demonstrated the involvement of the GID4/CTLH complex in the regulation of cell migration via recognition of the proline degron and degradation of a GTPase activating enzyme ARHGAP11A. Further, the work of Owens et al. 2023 implicated the GID4/CTLH complex in the interactions with proteins associated with RNA processing, transcription, splicing, and chromatin. Interestingly, although some interactors contain the Nt-Pro degron (e.g., DDX17, DDX21, DDX50) and compete for GID4 binding with PFI-7, the GID4-dependent degradation of these substrates was not observed. Furthermore, other detected interactors in this study did not contain the specific degron sequence nor were they degraded, pointing to the wide repertoire of GID4/CTLH functions.

In this work, we present the development of chemical probes interacting with GID4, utilizing Fragment-Based Screening (FBS) followed by a structure-guided approach. These efforts resulted in the development of a series of GID4 ligands that lock GID4 in distinct conformations. Three conformational states were identified based on the measured distances between mobile hairpin loops (L1-L4) and compared to the available crystal structures of GID4. Ultimately, the best compound, compound **14,** shows 23 nM affinity in biophysical assays and confirmed target engagement in cells. Furthermore, we additionally explored a suitable linker attachment point from compound 14 for the synthesis of bifunctional degraders. These findings deepen the understanding of GID4 binding pocket plasticity and constitute a valuable addition to the still scarce number of available GID4 chemical probes.

RESULTS

Identification of Compound 1 - fragment hit of GID4

To develop GID4-selective ligands, we employed biophysical screenings of a library of ~2200 fragments. For this purpose, two versions of the GID4 recombinant protein (amino acid region 116-300) were purified. One version was untagged, and the other contained the N-terminal Avi-tag. We used the untagged protein in the differential scanning fluorimetry (DSF), while the biotinylated Avi-tagged protein was utilized in surface plasmon resonance (SPR) experiments. To

confirm the integrity and activity of the GID4 protein, DSF was performed in the presence of c=50 µM endogenous degron peptide, PGLWKS. The untagged GID4 protein had a denaturation temperature of Tm = 61.5 °C and sigmoidal two-state transition, increasing to Tm = 62.4 °C in the presence of the peptide, confirming high stability of the well-folded protein species. The immobilization of the biotinylated version of GID4 on the SPR chip resulted in quality sensograms indicating the saturable binding of the PGLWKS degron peptide. The measured affinity of K_D^{GID4}=2.13 µM for the degron peptide was consistent with the literature data (Dong et al. 2018, S1). Next, we performed the DSF screen at a constant fragment concentration (c=500 µM) that revealed two hits. Among them, compound 1 has shown the highest shift of denaturation temperature (ΔTm = +2.6°C), which is an indicator of binding and consequent protein stabilization. In parallel, SPR was used as an orthogonal screening method. The primary binding level and dose-response screens revealed 28 fragments with K_D^{GID4} < 1 mM (hit rate ~1.3%), with both DSF-identified hits confirmed by SPR. The subsequent validation of hits confirmed compound 1 containing N,N'-disubstituted guanidine moiety as the strongest binder with the affinity of K_D^{GID4}=78.80 µM determined by the steady-state affinity binding model (Figure 1).

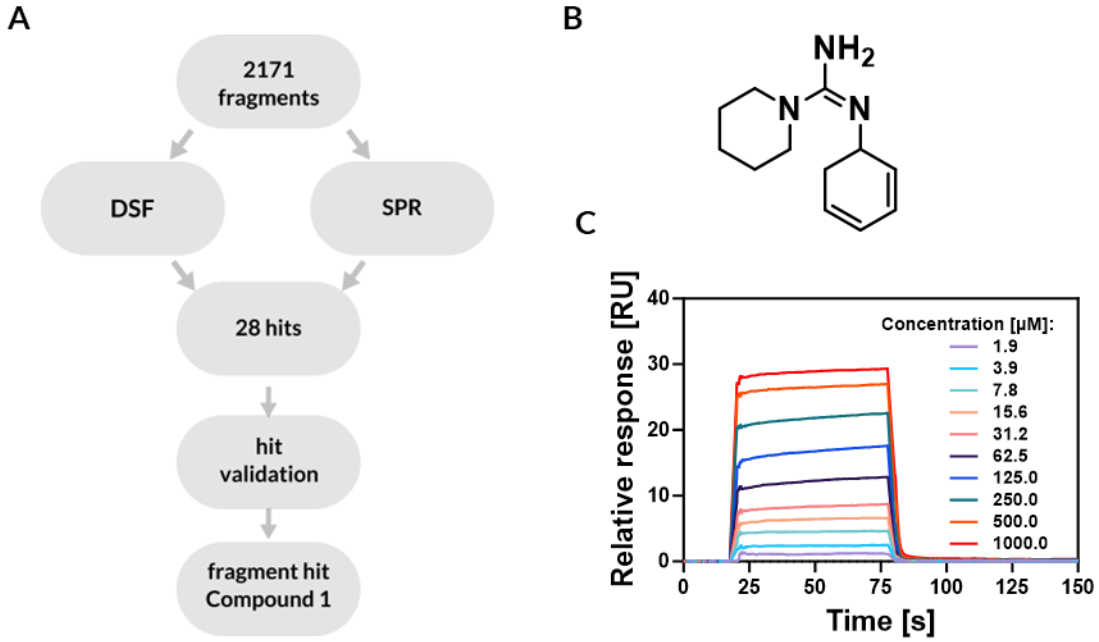

Figure 1. Identification of fragment hit compound 1. A) Workflow of hit identification, B) Chemical formula of compound 1. C) Representative SPR sensograms demonstrating binding of Compound 1 to the immobilized GID4. K_D^{GID4} was determined by a steady-state affinity binding model (N=3).

Next, to understand the binding of compound 1, we determined its co-crystal structure with GID4 (see Table S1 for X-ray diffraction data and model refinement statistics, PDB: 9QDX). As previously reported by Dong et al. 2018, GID4 is an antiparallel eight β-strand barrel linked with an insert of three α-helices. One end of the β-barrel contains a deep hydrophobic binding pocket surrounded by four loops: L1 (134-138), L2 (163-169), L3 (240-250) and L4 (275-279). These loops flanked a degron peptide binding pocket, which overlapped with the ligand site. Comparing the positions of loops L2 and L3 in the compound 1-bound structure and the degron-bound structure (PDB: 6CD9), loops L2 and L3 in the degron-bound form adopt a more 'closed-like' conformation, resulting in a tighter binding pocket compared to our hit-bound structure. (Figure S2F). The N, N'-disubstituted guanidine moiety of the hit compound interacted with the side chain of Glu237 (Figure 2). The same Glu237, highly conserved across many species (Dong et al. 2018) anchored the amino terminus degron peptide, for instance, proline, as reported in GID4 crystal structures (PDB: 6CDG, 6CD9, 6CDC). Additionally, the guanidine moiety was superposed with the pyrrolidine ring of proline from GID4 degron tetrapeptide PSRW (PDB: 6CD9). The piperidine of compound 1 was in proximity to GID4 Ser253 (~3.05 Å). The GID4 binding pocket was hydrophobic and was lined by Tyr273, Phe254, Leu171, Ala252, Leu164, Ile161, and Leu159 (Dong et al. 2020). The piperidine of compound 1 was placed between Tyr258 and Tyr273, with

which it formed hydrophobic contact. The phenyl group of the compound 1 further explored the hydrophobic pocket reaching towards Leu171, and Ile161 (Figure 2D).

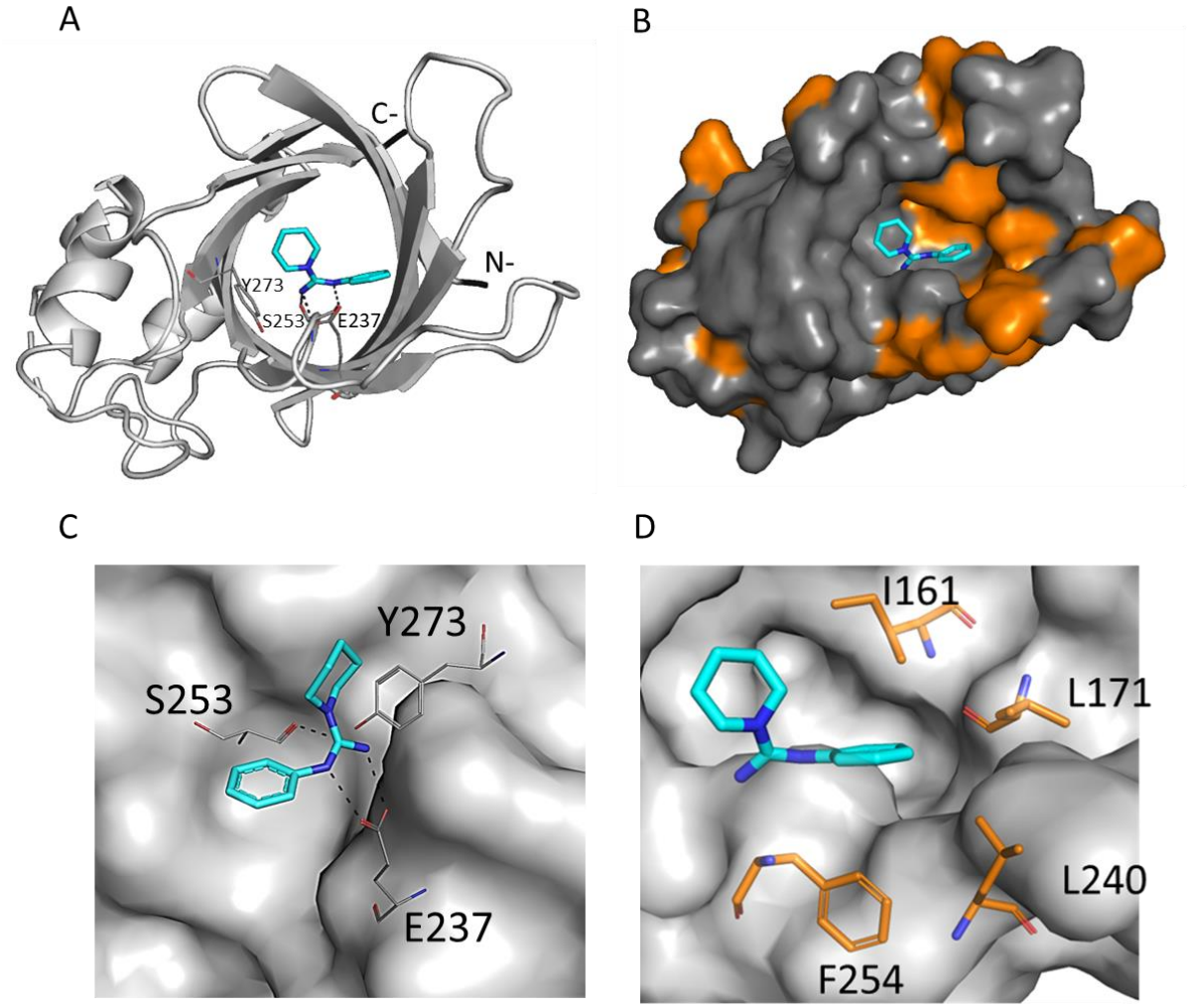

Figure 2. The crystal structure of GID4 in complex with compound 1 (PDB: 9QDX). A) Top view of GID4 binding pocket with compound 1 (turquoise) bound in the degron binding pocket, GID4 represented as cartoon (grey). The N- and C-termini of the protein are labeled as N and C, respectively. B) The surface representation of GID4 with all hydrophobic residues colored in orange (the rest of the amino acids are grey) with compound 1 (turquoise) bound in the GID4 binding pocket. The binding pocket has a hydrophobic character. C) Key interactions with Glu237, Ser253 and Y273 are labeled for reference. D) Close view of the hydrophobic pocket, where the phenyl moiety of compound 1 is surrounded by hydrophobic residues Ile161, Leu171, Leu240, and Phe254.

Development of GID4 ligand series

After identification of the binding pocket and key interactions of the fragment with GID4, we began synthesizing a series of analogs (Table 1). The changes in affinity were monitored using surface plasmon resonance and differential scanning fluorimetry. The monohalogenated analogs (compounds **2** and **3**) validated the series as a starting point for hit expansion. The corresponding 3-chloro-5-fluorophenyl derivative showed comparable potency to compound **3**. Exploration of the piperidine substitution pattern indicated that methyl substitutions improved affinity towards GID4 with the most prominent result at positions 2 and 4. In the next step, we replaced the 3-Cl group to find an additional potency boost. Screening of various scaffolds revealed significant improvement in the binding affinity for 5-methyl furan-2-yl substituent, especially when combined with a 4-Me piperidine ring (Table 1, compound **9**).

Table 1. Binding to GID4 by analogs of compound 1.

Compound	Chemical structure	ΔTm by DSF (°C)	KD by SPR (μM)
2	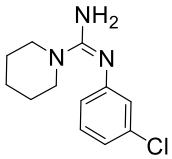	1.6	23.00
3	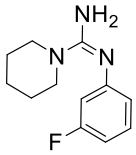	3.3	12.00
4	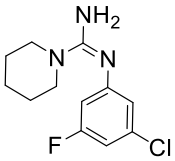	2.8	8.16
5	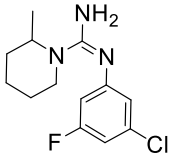	3.3	2.87
6	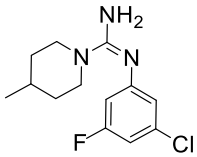	3.2	2.94

7	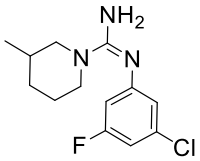	3.3	4.12
8	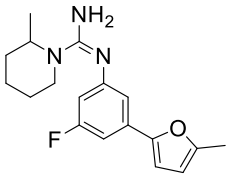	4.3	0.94
9	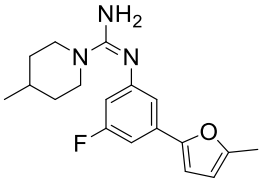	4.5	0.73

To further understand the tighter binding of compound **9**, we determined its crystal structure in a complex with GID4 (Figure 3, PDB: 9QDYFigure 3. The crystal structure of GID4 protein in complex with compound 9 (PDB: 9QDY). A) Top view of GID4 binding pocket with compound 9 (magenta) bound in the degron binding pocket, GID4 represented as cartoon (grey). The N- and C-termini of the protein are labeled as N and C, respectively. B) The surface representation of GID4 with all hydrophobic residues colored orange (the rest of the amino acids are grey) with compound 9 (magenta) bound in the GID4 binding pocket. The binding pocket has a hydrophobic character. C) Key interactions with Glu237, Ser253, and Y273 are labeled for reference. D) Close view of the hydrophobic pocket, where the phenyl and furan moieties of compound 9 are surrounded by hydrophobic residues Ile161, Leu171, Leu240, and Phe254.). Its guanidine moiety interacts with the side chain of Glu237 and aligns with Glu237 from the compound **1** structure. Compound **9** extends beyond the canonical peptide cavity to reach Leu171, Tyr168, and Thr173 on the other side of the binding pocket not occupied by the peptidic degron. This side of the pocket is lined with hydrophobic residues, which interact with the furan and piperidine moieties through hydrophobic interactions (Figure 3D). Similarly, to compound 1, the piperidine of compound **9** forms hydrophobic contacts with two tyrosine residues by forming a sandwich with Tyr258 and Tyr273 within the hydrophobic part of the GID4 binding pocket. The tighter binding of compound **9** over compound **1** could be due to more extensive hydrophobic interactions and possibly further

stabilization by a strong polar interaction with Glu237. Furthermore, in the compound **9**-bound structure of GID4, loops L2 and L3 have similar positions to compound **1**-bound GID4 (Figure S2F).

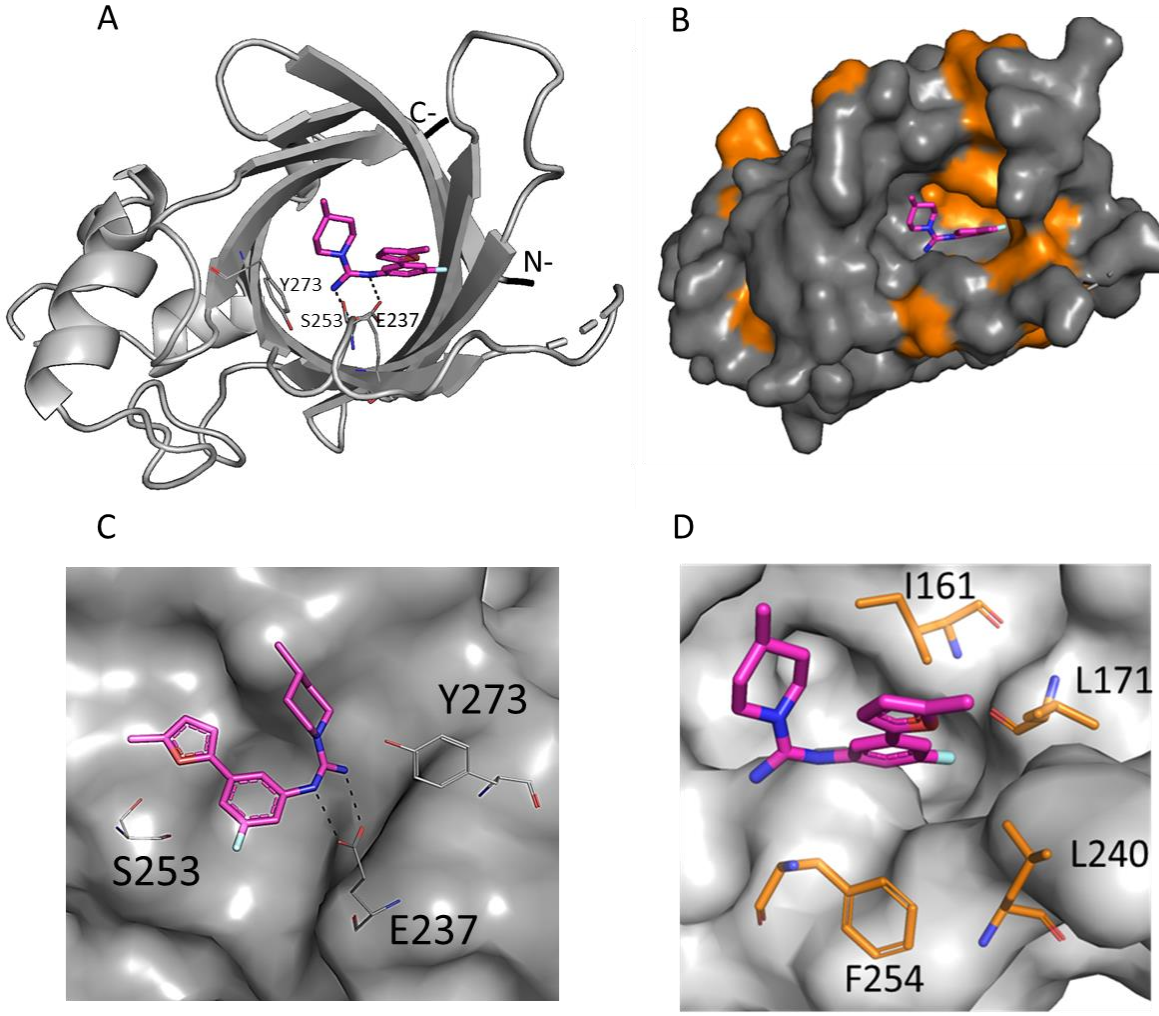

Figure 3. The crystal structure of GID4 protein in complex with compound 9 (PDB: 9QDY). A) Top view of GID4 binding pocket with compound 9 (magenta) bound in the degron binding pocket, GID4 represented as cartoon (grey). The N- and C-termini of the protein are labeled as N and C, respectively. B) The surface representation of GID4 with all hydrophobic residues colored orange (the rest of the amino acids are grey) with compound 9 (magenta) bound in the GID4 binding pocket. The binding pocket has a hydrophobic character. C) Key interactions with Glu237, Ser253, and Y273 are labeled for reference. D) Close view of the hydrophobic pocket, where the phenyl and furan moieties of compound 9 are surrounded by hydrophobic residues Ile161, Leu171, Leu240, and Phe254.

Encouraged by this observation, we continued the optimization of compound **9** (Table 2). The introduction of another methyl group at position 4 of piperidine led to an improved affinity of

compound **10** (K_D^{GID4}=0.21 μM). However, one notable potential liability presented by this compound was its known furan metabolic instability (Dalvie et al. 2002). Therefore, efforts were focused on the substitution of the furan and the identification of analogs with improved potency and stability. For this purpose, a set of molecules containing amide derivatives in position 4 of the furan ring has been synthesized. Among all tested compounds, **12,** bearing a dimethyl amide group stood out as a potent GID4 ligand with a 4-fold improved potency. Secondary amides possessing an additional hydrogen bond donor displayed inconsistent binding by either retaining the affinity of compound **10**, i.e. compound **11,** or losing it significantly, compound **13**. As a final step in hit optimization, we decided to examine a variety of tertiary amides and assess the influence of ring size and heteroatom type on the binding mode. From these efforts, we found that the piperidine derivative, compound 14, showed a 2-fold improvement in potency compared to compound **12**, whereas the pyrrolidine analog, compound **17**, exhibited nearly a 2-fold loss in activity. Moreover, replacing carbon at position 4 of the piperidine ring with other heteroatoms (O, N) reduced activity towards GID4. Notably, the strongest compound in the series (compound **14**, K_D^{GID4}=0.03 μM) is over 2500-fold more potent GID4 binder than the parent hit compound 1 (K_D^{GID4}=78.80 μM).

Table 2. SAR of substituents at C4 of the furan ring.

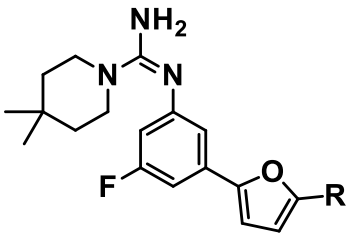

Compound	R	dTm by DSF (°C)	KD by SPR (μM)
10	CH_3	5.4	0.21
11	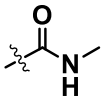	4.8	0.31
12	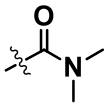	6.9	0.06
13	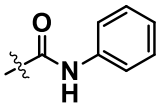	3.9	1.43

14	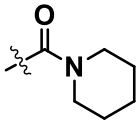	7.7	0.03
15	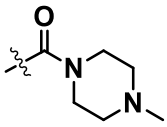	5.9	0.12
16	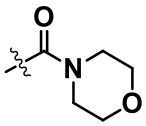	6.2	0.09
17	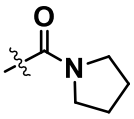	6.7	0.10

Finally, to explain the affinity boost, we determined the crystal structure of GID4 bound to compound **14** to understand the binding of this ligand to the protein (PDB: 9QDZ). A guanidine moiety of compound **14** interacted with the side chain of Glu237 and superposed with Glu237 from the structure of compound **1**. Similarly to compound **9**, compound **14** extends beyond the canonical peptide cavity, as its furan and piperidine ring moieties point towards Leu171, Tyr168, and Thr173 (Figure 4), exploiting the other side of the binding pocket, not occupied by the N-degron. Compound **14** interacts with an even bigger surface of the binding pocket compared to compound **9**, making more contact with the amino acid side chains. Within the hydrophobic binding pocket of GID4, the ligand forms hydrophobic interactions with Tyr258 and Tyr273. Moreover, in the compound 14-bound form, the piperidine side chain of the guanidine moiety, which superimposes with the second residue of the degron peptide-bound form, reaches towards Ser235. Loops L2 and L3 have a similar position to compound 1 bound GID4 (Figure S2F). The higher affinity of compound 14 compared to compounds 9 and 1 is likely due to an additional interaction with Ser135, extensive hydrophobic contacts within the hydrophobic pocket, and further stabilization through polar interactions with Glu237.

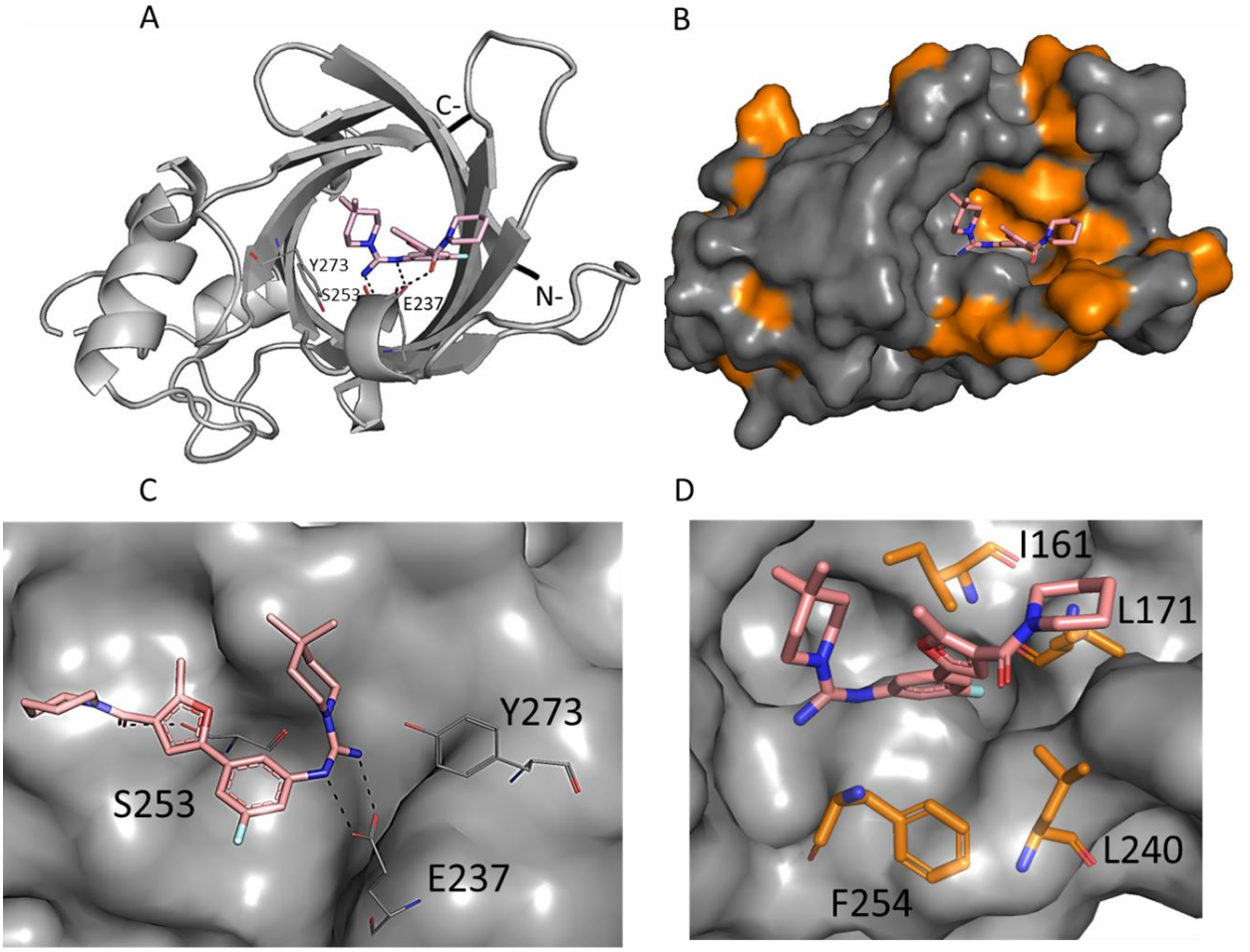

Figure 4. The crystal structure of GID4 protein in a complex with compound 14 (PDB: 9QDZ). A) Top view of GID4 binding pocket with compound 14 (salmon) bound in the degron binding pocket, GID4 represented as cartoon (grey). The N- and C-termini of the protein are labeled as N and C, respectively. B) The surface representation of GID4 with all hydrophobic residues colored orange (the rest of the amino acids are grey) with compound 14 (salmon) bound in the GID4 binding pocket. The binding pocket has a hydrophobic character. C) Key interactions with Glu237, Ser253 and Y273 are labeled for reference. D) Close view of the hydrophobic pocket, where the phenyl and furan moieties of compound 14 are surrounded by hydrophobic residues Ile161, Leu171, Leu240, and Phe254.

Identification of the exit vector in GID4 ligands

Our next aim was to identify a suitable linker attachment point from compound **14** for the synthesis of bifunctional degraders. We sought to exploit two exit vectors from piperidine (positions 3 and 4) as presented in Table 3. The overall binding affinity of tested compounds **18-23** was determined to be weaker compared to compound **14** with a slight preference towards 3-

substituted derivatives represented by racemic mixtures. Three different substitution patterns *i.e.* methoxy, 2-(2-methoxyethoxy) ethyl, and 1-(4-methylpiperazin-1-yl) ethan-1-one revealed affinity in the range of K_D^{GID4}=0.05 to 0.14 μM as measured by SPR. To understand if the binding of ligands extended with linkers introduced any additional interactions with the protein, we determined the crystal structures of compounds 18, 21 and 33 in a complex with GID4 (PDB: 9QZG, 9QZI and 9QZH, respectively). Unfortunately, in all three cases, the ligand parts beyond furan moieties were not supported by electron density (Figures S4-S6) as they were mobile and pointed outside of the solvent-exposed binding pocket. In the cases of compounds 21 and 33, we set the occupancy of the linker atoms to zero to avoid misleading structural interpretations. As a result, the exact position of linker extensions was not determined and should be taken with approximation (Figure S7 and S8). Additionally complexes of GID4/compound 33 crystallized with four units of protein in one asymmetric unit (instead of one protein chain in all other cases) and only two of them (chain C and Chain D) had ligand bound. Nevertheless, all tested compounds remained active and proved their utility as building blocks for the bifunctional degraders.

Table 3. Further modifications of the piperidine moiety in compound 14 and assessment of potential exit vector for bifunctional degraders.

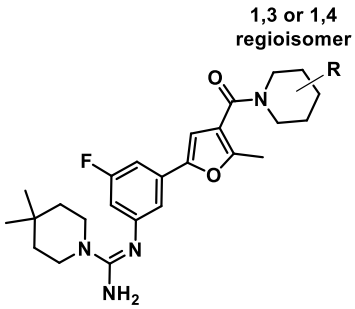

	R	Regioisomer	dTm by DSF (°C)	KD by SPR (μM)
18		1,4	7.1	0.13
19		1,3	7.1	0.05
20		1,4	6.5	0.05
21		1,3	6.8	0.05
22	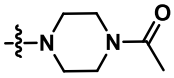	1,4	5.9	0.14
23		1,3	6.4	0.09

Intracellular GID4 engagement assay

Next, we investigated the cellular activity of the developed GID4 binders. For this purpose, we generated a HEK293T cell line, stably expressing the full-length GID4 protein containing the N-terminal HiBiT tag. Cells were incubated with either a DMSO vehicle or ligands for 1h, and the luminescence readout was performed while ramping the temperature from 40.4 to 63.5°C. The temperature of aggregation (Tagg) was determined at 50% of the maximal signal. For the reference sample treated with the DMSO vehicle, the $Tagg_{(DMSO)}$ was established at 54.5 °C. Compounds interacting with GID4 lead to the stabilization of the protein and a rise in Tagg. This way, the assay validates target engagement in cells and indirectly implies the cell membrane permeability. For each ligand we derived a parameter of ∆Tagg that is the difference between $Tagg_{(ligand)}$ and $Tagg_{(DMSO)}$. Exemplary denaturation curves are depicted in Figure 5A. While hit compound 1 did not stabilize the protein *in cellulo*, a gradual shift of Tagg was observed for compounds **2**, **9**, and **14**. Compound **14** gave one of the highest readouts with ∆Tagg = + 3.6 °C reflecting efficient target engagement in cells. To confirm the on-target action of compound **14**, we synthesized a negative control, which maintained similar physicochemical properties but was incapable of interacting with GID4. In this compound, the amine group responsible for binding with Glu237 was modified with the ter*t*-butyloxycarbonyl group, which precluded the interaction with GID4. Indeed, no intracellular target engagement was observed for this modified compound. Figure 5B shows the correlation between ∆Tm obtained from the biophysical experiment DSF and values of ∆Tagg in the cellular experiment. As expected, there was a clear correlation between the stabilization of GID4 *in vitro* in the DSF and in cells where higher ∆Tm predicts a more efficient target engagement. A few outliers were observed from this trend (Figure 5B, purple squares) that could indicate worse cell membrane permeability (higher cLogP) or compound instability in the cellular medium related to the furan ring. Importantly, all tested analogs with the additional linker fragments (compounds **18-23**) retained activity in the target engagement assay, with higher thermal shift values ∆Tagg observed for flexible PEG linkers (compounds **20** and **21**) compared to rigid substitutions (compounds **22** and **23**).

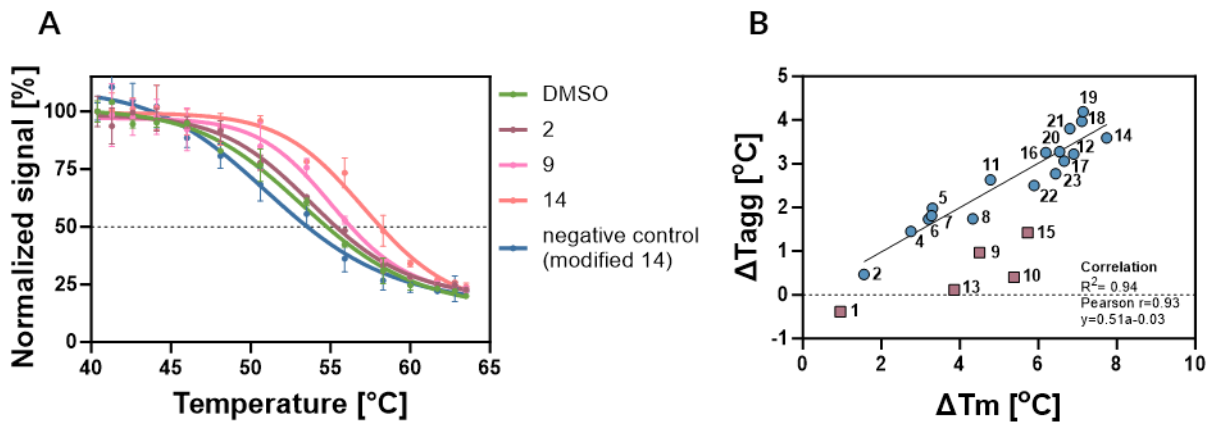

Figure 5. Intracellular target engagement assay. A. Denaturation curves obtained from cells treated with selected GID4 binders (compound 2, 9, 14 and negative control of 14). Data presented here are the mean ± s.d. of two independent experiments, run in duplicates. B. Correlation between ΔTm (DSF) and ΔTagg (intracellular GID4 engagement assay) values obtained for GID4 binders. Compounds are indicated by numbers. Outliers are marked as purple squares and were not included in the calculation of the Pearson correlation coefficient (r).

Synthesis of GID4-BRD4 bifunctional degraders

After confirmation of target engagement in cells, we next assessed the ability of GID4 to induce targeted protein degradation by synthesizing representative examples of GID4-BRD4 bifunctional compounds. For this purpose, we utilized our best ligand **14** together with a well-known BRD4 ligand JQ1 and explored a set of standard linkers with various exit vectors and lengths: either rigid, 2xPEG, or 4xPEG (Figure 6A). Compound **26** was synthesized as a direct analog of **24** containing inactive (-)-JQ1 enantiomer to provide a negative control for our assays. We assessed binary interactions with both proteins, GID4 and BRD4, as well as the formation of the ternary complex by SPR and HTRF (Figure 6 and Table S2). All compounds except for **26** retained high affinity to BRD4 (K_D^{BRD4} in the range of 0.006-0.02 µM) while binding to GID4 was weakened in comparison to sole GID4 ligand (K_D^{GID4} in the range of 0.32-0.63 µM for bifunctional compounds vs K_D^{GID4} =0.03 µM for compound **14**). Most importantly, all bifunctional degraders with active BRD4 warhead mediated ternary complex formation between GID4 and BRD4 as assessed in HTRF and/or SPR (Figure 6 B-C). Next, bifunctional compounds were tested in the NanoBRET assay to confirm their interaction with the BRD4 in intact and lysed cells (Table S2). All compounds, except

for negative control **26**, engaged BRD4. Notably, significantly higher pEC_{50} values were obtained in the lytic mode (EC_{50}=0.05-0.08 µM) compared to the live mode (EC_{50}=0.40-2.51 µM), indicating potential permeability issues or high efflux. Despite the engagement of BRD4, none of the synthesized degraders stabilized GID4 in the intracellular engagement assay, resulting in negative ΔTagg values (Table S2). This was consistent across all compounds, regardless of linker length and composition or the exit vector used. Consequently, due to the lack of interaction with GID4 in cells, we did not observe BRD4 degradation.

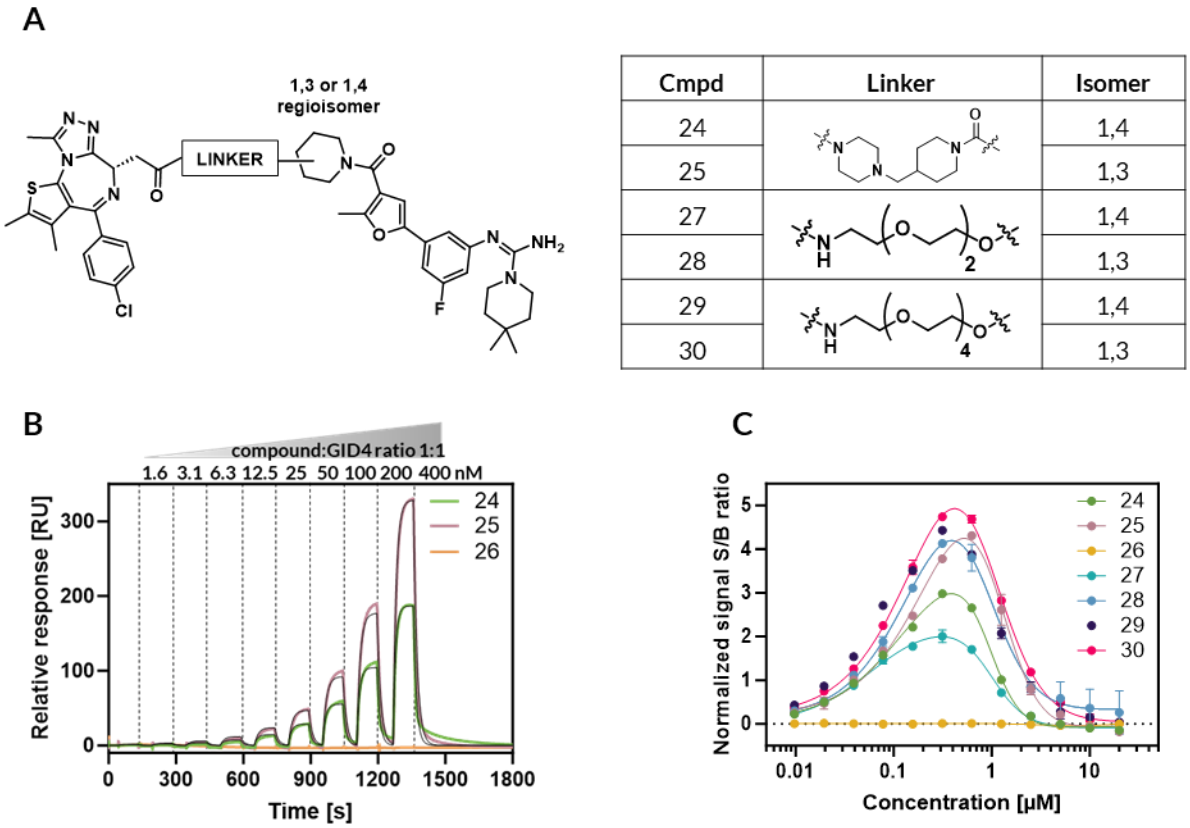

Cmpd	Linker	Isomer
24		1,4
25		1,3
27		1,4
28		1,3
29		1,4
30		1,3

Figure 6. Synthetized GID4-based bifunctional degraders mediate ternary complex formation between GID4 and BRD4. A) Structures of synthesized bifunctional degraders and corresponding linkers. B) Examples of SPR sensograms of ternary complexes between immobilized BRD4/bifunctional degrader/GID4 for selected compounds. C) HTRF assay as an orthogonal method for confirmation of ternary complex formation. Only negative control 26 does not mediate the formation of the BRD4/GID4 complex.

Observed variabilities of GID4 loops

During the ligand optimization process, we resolved 49 high-resolution X-ray structures of GID4-ligand complexes. Intrigued by the reported conformational flexibility of GID4 (Chrustowicz et al. 2022; Chana et al. 2022; Dong et al. 2018), we used our X-ray data as well as the available GID4 structures to explore the behavior of the flexible loops (L1-L4) in proximity to the ligand/peptide binding pocket. Analysis of the flexible regions in crystal structures of GID4-ligand complexes revealed significant variabilities, particularly in loops L2-L3, reminiscent of the major variances observed in the apo- and holo- states described by Dong et al. 2018. To investigate the variability of these loops, we performed clustering to delineate distinct structural patterns. By calculating all pairwise distances between the residues of loops, we aimed to capture the intricate variations in L1-L4. To simplify the analysis and facilitate further interpretation, we leveraged principal component analysis (PCA) to reduce the dimensionality of the data. From the PCA results, we extracted the most critical components, PC0 and PC1, which represented the primary sources of structural variability among the proteins. Interestingly, two key distances, d_0 and d_1, emerged from PC0 and PC1: namely d_0 (T165-S250; L2-L3) and d_1 (H244-E279; L3-L4). These distances were then utilized as representative measures of structural variability for subsequent analysis and visualization. By focusing on these key distances, we effectively captured the essential features of the loops' positions while reducing the data complexity. Clustering based on distances d_0 and d_1 yielded three distinct clusters among the conformers, C1, C2, and C3 as illustrated in Figure 7.

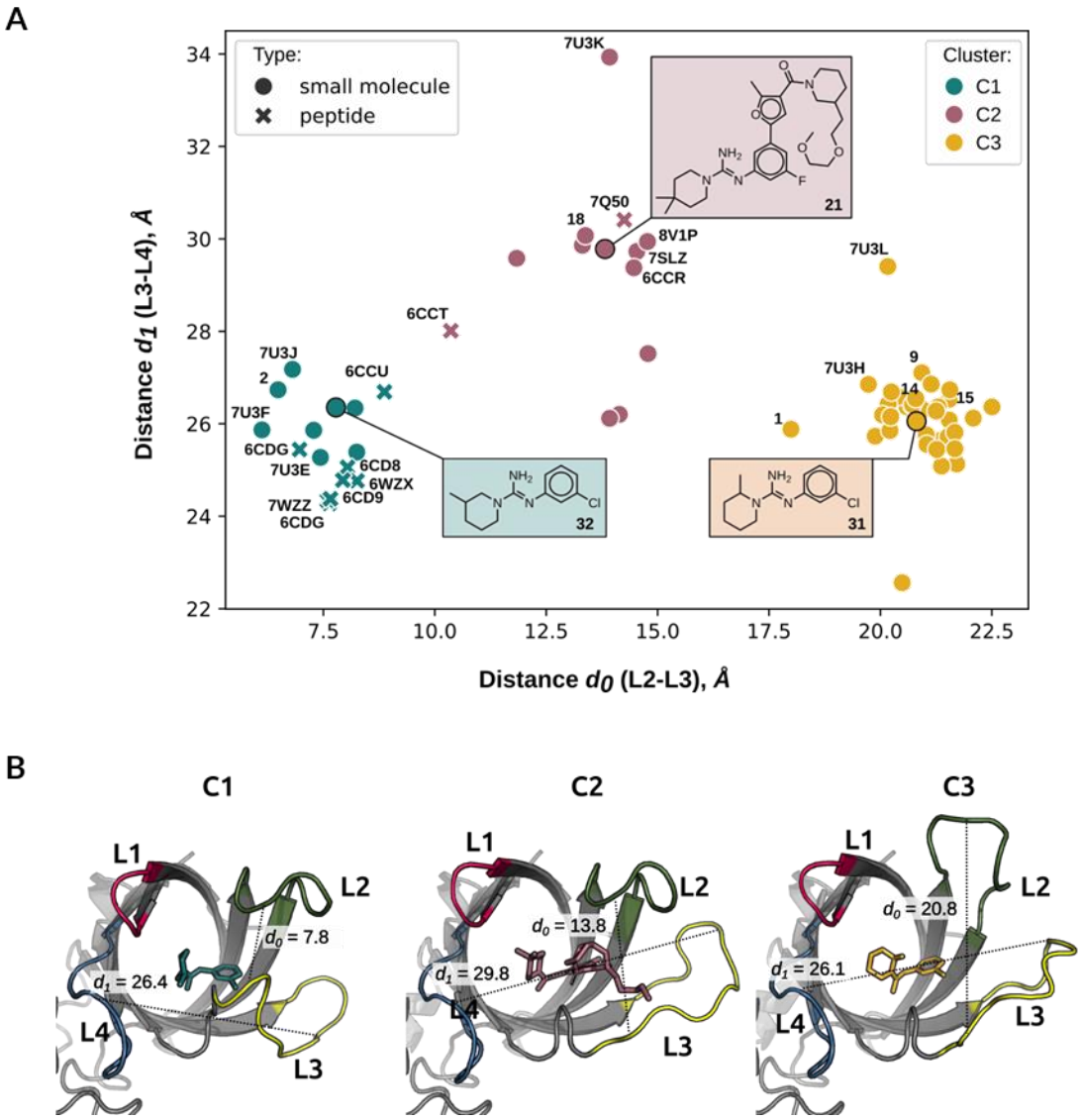

Figure 7. Conformational flexibility of GID4. A) GID4 structural variability and ligand-induced states. The plot in the distance coordinates between residues d_0 (L2-L3; T165-S250) on the x-axis and d_1 (L3-L4; H244-E279) on the y-axis. Each point in the plot corresponds to the individual protein structure (in-house data or PDB data). The color of the points indicates the cluster assignment (C1, C2, C3). Representatives of each cluster are marked with black edge colors and are presented in B. B) Representatives of protein-ligand complexes from each cluster: C1 - closed conformation with compound 32, C2 - semi-open conformation with compound 21, C3 - open conformation with compound 31.

The distinctive structural feature of the clusters was the 'openness' of the binding pocket, with a significantly visible difference in the orientation of L2 and L3 (which is also aligned with distances d_0, d_1) (Figure 7). Each conformer, derived from a complex with a specific binder, allowed for the examination of structural features associated with the cluster. Cluster C1 contained structures

with a fully closed arrangement of the loops, L2 and L3 as illustrated in Figure 7B. For example, almost all peptide binders belonged to cluster C1 (the only exceptions are structure 6CCT - PTLV peptide, (Dong et al. 2018) and 7Q50 - FDVSWFM peptide (Chrustowicz et al. 2022). In addition, cluster C1 accommodates small molecule ligands with a size of ≤20 heavy atoms. The absence of bulky groups in these ligands appeared to promote a close conformation of loops L2 and L3. In contrast, the structures of cluster C2 are semi-open, characterized by a different orientation of L3 (example in Figure 7B). Our exploration into loop rearrangements within protein-ligand complexes unveiled the potential role of the position of aromatic substituents in semi-open structures represented by cluster C2. We suggest that the presence of aromatic groups in proximity to L3 may cause rearrangement of that loop. This observation aligns with previous research by Chrustowicz et al. 2022, who noted the ability of peptide binders featuring a unique large N-terminal residue (phenylalanine), to induce diverse loop arrangements, *e.g.*, peptide binder 7Q50 with a sequence of FDVSWFM. It is worth noting that the second peptide 6CCT (sequence PTLV), which belongs to the cluster C2 does not possess the bulky group at this position. However, it is positioned at the border between clusters likely due to low-resolution crystal structures, leaving some L3 loop residues unresolved. Interestingly, our findings extended beyond our dataset of LMW binders, as small molecules from publicly available structures, *e.g.*, 7SLZ (PFI-7, Yazdi et al. 2023) and 8V1P also exhibit aromatic groups at analogous positions to the aforementioned Phe residue. Only a structure represented by 7U3K (compound 89 from Chana et al. 2022) stands as an outlier, with an aliphatic chain occupying the position typically reserved for aromatic groups. This structural divergence, evident from its distances from the cluster centroid (d_0=13.9, d_1=33.9, see Figure 7A), underscores the unique conformational landscape of this ligand-binding interaction. Interestingly, the structures in cluster C3 exhibit an open conformation, attributed to movements of both L2 and L3 (Figure 7B). Despite exhaustive efforts, no clear patterns have emerged to explain the fully open conformation observed in this cluster. Unlike clusters C1 and C2, there seems to be a lack of discernible structural elements or binding motifs that universally characterize this group. This intriguing observation suggests that the structural dynamics within this cluster may be driven by a complex interplay of factors that are yet to be fully understood. It is worth noting that our best GID4 ligand **14** and the benchmark compound PFI-7 (7SLZ) induce different GID4 conformations, C3 (open) and C2 (semi-open), respectively.

DISCUSSION

Our study has identified compound **14** as a potent GID4 binder, demonstrating significant activity in intracellular target engagement assays. When comparing compound **14** to another recently revealed chemical probe, PFI-7, both exhibit similar affinity for GID4 and comparable molecular properties. Considering these ligands as potential GID4 warheads for bifunctional degraders, their high molecular weight and logP values place them in a less bioavailable space, similar to VHL ligands, rather than small and readily bioavailable CRBN ligands (Maple et al. 2019). Indeed, the BRD4 NanoBRET assay showed higher pEC_{50} values in the lytic mode in comparison to the life mode (Table S2), indicating poor cell membrane permeability or high efflux of the GID4-based bifunctional compounds presented in this manuscript. Nevertheless, the most effective design and structural optimization of the linker can mitigate the less favorable physicochemical properties of the E3 ligase ligand, as presented for the PFI-7 probe. Bifunctional degraders, based on PFI-7 warhead, were shown to decrease BRD4 levels *in vitro* and *in vivo* (Li et al.2025). The authors, however, underline the importance of the linker length as well as the cell-type-specific activity of developed degraders. Introducing additional intramolecular interactions within the degrader molecule may also help to overcome suboptimal molecular properties of a ligand by promoting folding that masks polar regions in a nonpolar environment. This conformational flexibility of so-called molecular chameleons can facilitate cell membrane permeability (Atilaw et al. 2021). A similar strategy was shown for the VHL-based SMARCA2 degrader where authors, by linker optimization, achieved reduced efflux and acceptable oral bioavailability of F=22% (Kofink et al. 2022).

In case of compound **14**, despite the interaction with BRD4 in cellular experiments and the successful mediation of the ternary complex *in vitro* (Table S2), our attempt at GID4 recruitment by the bifunctional degraders was unsuccessful. This might be explained by a more than tenfold reduction in affinity of the bifunctional compounds for GID4 compared to compound 14 alone. It is likely that the combination of reduced affinity and poor permeability was sufficient to achieve a lack of efficient engagement of GID4 inside the cell. In consequence, we did not observe degradation of BRD4. This outcome underscores the necessity for further refinement of the chemical structures of GID4 bifunctional compounds to enhance their cell membrane permeability and increase their affinity to GID4. A limitation of the assessment of the degradation potential of

the created bifunctional compounds is that it focuses on a single target (BRD4) in one cell line (HEK293) and does not include an assay to evaluate ternary complex formation in a cellular context. Incorporating such an assay in future work could provide valuable insights for optimizing bifunctional compounds with respect to exit vector orientation, linker length and composition, and selection of compatible degradation targets.

More work is needed to better understand the mechanisms of GID4-mediated degradation and GID4/CTLH complex regulation. What becomes an eminent feature of mammalian E3 ligase complexes are the mimicry-type of regulatory mechanisms that modulate the access of degrons from *bona fide* substrates to the binding pocket (Gottemukkala et al. 2024, Yi et al. 2024). A growing body of evidence suggests that GID4 has multiple interaction partners including those not containing the canonical Pro-N degron motif (Bagci et al. 2023; Owens et al. 2023). This fact may be supported by the observed substantial mobility of GID4 loops—particularly L2–L3—which might account for the ability to accommodate various interactors within the binding pocket.It has been previously demonstrated that the flexible regions of protein structures play a pivotal role in facilitating protein-protein interactions, enabling the recognition of multiple targets at a single molecular surface (Sundberg et al. 2000) and that an intrinsic disorder can serve as the structural basis for protein promiscuity (Dunker et al., 2005). Our study substantially expands the repertoire of ligands capable of inducing distinct GID4 loop conformations. Prior to this work, only a single example of an open-loop structure (cluster C3), represented by structure 7UH3 (Chana et al. 2022), has been reported. In contrast, our investigation has yielded over 30 additional structures exhibiting similar open-loop conformations. Notably, our most potent binder, compound **14**, also belongs to cluster C3, whereas the benchmark compound PFI-7 induces a semi-open loop configuration.

Interestingly, a similar conformational flexibility was observed for CRBN where authors demonstrated that molecular glues inducing a closed form of CRBN are more efficacious in target degradation. Inspired by this notion, we theoretically examined a second modality in TPD, namely molecular glues. At present, only a few ligases with molecular glue abilities are known (*e.g.*, CRBN or DCAF15). To measure the probability that C1, C2 and C3 conformations of GID4 form molecular glue-mediated ternary complexes, we plotted the pocket volume against the calculated protein-protein interface (PPI) by using a small dataset of structures comprising popular ligases in targeted protein degradation and proteins known to interact with molecular glues (Figure S8) (Rui

et al. 2023). Such analysis has shown distinct grouping of proteins with known molecular glues. For instance, CRBN has a high PPI value and a mid-size binding pocket. Moreover, the closed form of CRBN ($CRBN^{C}$) has a higher PPI value than the open form ($CRBN^{O}$). This finding correlates with the experimental knowledge - findings of Watson et al. 2022 and Yan et al. 2023 suggest that the CRBN-molecular glue complex indeed contains CRBN in the closed form, which is essential for its function in protein degradation. On the other hand, ligases with low PPI and large binding pockets are challenging for the development of molecular glues. VHL is generally considered unsuitable for molecular glue strategies; nevertheless, one confirmed case of a molecular glue-induced complex between VHL and CDO1 has been reported (Tutter et al. 2025). We explored centroids of all three types of conformation for GID4 protein (C1, C2 and C3). The open form of GID4 (cluster C3) is the closest to the proteins capable of forming molecular glue-mediated complexes. Overall, understanding the complexity and structural features of the CTLH complex can aid in designing novel molecular glues involving ligases like GID4 in the future.

CONCLUSIONS

This work validates fragment-based lead generation supported by structural analysis as a powerful approach in drug discovery. We used standard biophysical methods such as SPR and DSF for hit identification and validation as well as subsequent structure-guided growth of the fragment hit. This resulted in the development of potent GID4 ligand with identified exit vectors and confirmed activity in the intracellular target engagement assay. In addition, our analysis offers comprehensive insight into structural flexibility of GID4. The distinctive clusterization of the ligand-GID4 complexes might be helpful in better understanding of the structure-activity relationship and design of new ligands to achieve desired properties and therapeutic outcomes. These findings provide a robust foundation for further exploration into the therapeutic potential of GID4 in targeted protein degradation and beyond.

MATERIALS AND METHODS

Recombinant protein expression and purification

GID4 expression and purification

Human Glucose-induced degradation protein 4 homolog (Gid4, UniProt ID: Q8IVV7) residues 124-289 were cloned into a vector to generate a N-terminal 6xHis-SUMO-tag for crystallography studies, residues 116-300 were cloned into a vector to generate a N-terminal 6xHis-SUMO-tag for DSF studies and residues 116-300 were cloned into a vector to generate a N-terminal Strep-SUMO-3C-6xHis-AVI-tag for SPR experiments. All constructs were verified by sequencing. Protein was expressed by transforming plasmid into chemically competent recombinant *E. coli* BL21(DE3) strain. *E coli* was cultured in LB medium supplemented with 50 µg/mL kanamycin in shaker flasks at 37°C and 160 rpm. Once an optical density at 600 nm (OD_{600}) reached 0.5-0.6, protein expression was induced by addition of 0.1 mM IPTG. Cultures were subsequently incubated overnight at 16°C at 90 rpm before harvesting by centrifugation at 6000 *g* for 20 minutes at 4°C. Cell pellets were stored in −80 °C until purification. To purify protein, pellets were thawed and resuspended in 150 mL of lysis buffer (50 mM Tris/HCl pH 8.0 at 4°C, 300 mM NaCl, 5% glycerol) supplemented with 10 mM β-ME (2-Mercaptoethanol), 1 mM PMSF (Phenylmethanesulfonyl fluoride), 0.5 mM EDTA, cOmplete™protease inhibitors cocktail tablet (Roche) and Pierce™ Universal Nuclease. Samples were subsequently lysed using EmulsiFlex cell disruptor by passing twice through it to maximize cell disintegration at 20,000-25,000 Bar. Afterwards 0.1% of polyethyleneimine was added. The resulting lysate was centrifuged at 30,000 *g* at 4°C for 30 minutes. Clarified lysates were incubated for 1 hour either with 10 mL of Ni Sepharose 6 FF resin equilibrated in 50 mM Tris/HCl pH 8.0 at 4°C, 300 mM NaCl, 5% glycerol, 10 mM β-ME and 5 mM imidazole for His-tag proteins or with Streptactin®XT 4Flow®High Capacity (IBA Lifesciences) resin equilibrated in 50 mM Tris/HCl pH 8.0 at 4°C, 300 mM NaCl, 10% glycerol, 10 mM β-ME for Strep-tag protein. After incubation the resin was loaded into an empty gravity flow column, the unbound fraction was collected and subsequently the resin was washed with either 10 CV of 50 mM Tris/HCl pH 8.0 at 4°C, 300 mM NaCl, 5% glycerol, 10 mM BME followed by 20 mM imidazole for His-tag proteins or 10 CV of 50 mM Tris/HCl pH 8.0 at 4°C, 300 mM NaCl, 10% glycerol, 10 mM BME for Strep-tag protein. Finally, bound protein was eluted using 30 ml of 50 mM Tris/HCl pH 8.0 at 4°C, 300 mM NaCl, 5% glycerol, 10 mM BME and 300 mM imidazole for His-tag proteins. For Strep-tag protein, the bound fraction was eluted using 30 ml of 50 mM Tris/HCl pH 8.0 at 4°C, 300 mM NaCl, 10% glycerol, 10 mM BME and 5 mM biotin. Protein was cleaved overnight at 4°C using 1:100 (Protease:POI) either Ulp-1 SUMO protease (for crystallography and DSF experiments) or with HRV-3C protease for SPR experiments. Proteins with His-tag in the same time were

dialysed to buffer containing 50 mM Tris/HCl pH 8.0 at 4°C, 300 mM NaCl and 10 mM β-ME. Cleaved proteins were further purified by reverse IMAC using HisTrap HP column (Cytvia), where flow through containing cleaved protein was collected, followed by size exclusion chromatography using HiLoad Superdex75 26/600 (Cytvia) equilibrated in 20 mM Tris/HCl pH 7.5 at 4°C, 100 mM NaCl, 0.5 mM TCEP for crystallography or in PBS supplemented with 1 mM DTT for DSF experiments. When needed for SPR experiments sample after cleavage was biotinylated using 0.05 mg/mL BirA enzyme in the buffer supplemented with 150 µM biotin, 5 mM $MgCl_2$ and 2 mM ATP. Biotinylation experiments were performed overnight at 4°C. Following biotinylation, protein was subjected to size exclusion chromatography equilibrated in PBS supplemented with 1 mM DTT. Selected fractions were analyzed by SDS-PAGE. Protein purity was evaluated by Coomassie-stained SDS-PAGE. Fractions corresponding to pure GID4 protein were pooled and flash frozen using liquid nitrogen and stored at −80°C.

BRD4 expression and purification

Human wild type Bromodomain-containing protein 4 (BRD4, UniProt ID: O60885) residues range 444-168 were cloned in a vector producing a N-terminal 6xHisTag and TEV protease cleavage site, and C-terminal AviTag. The construct was verified by sequencing. Protein was expressed in *E. coli* BL21(DE3) in Luria Bertani medium (LB) supplemented with 50 µg/mL kanamycin at 37°C. Once OD_{600} reached 0.5, the temperature was reduced to 16°C, and protein production was induced using 0.1 mM IPTG and incubated overnight. Cells were harvested and cell pellets were stored in −80°C until purification. To purify protein cell pellets were thawed and resuspended in lysis buffer containing 50 mM Tris/HCl pH 8.0 at 4°C, 150 mM NaCl, 5 mM imidazole and supplemented with 1 mM DTT, 0.5 mM EDTA, cOmplete™protease inhibitors cocktail tablet (Roche) and 5U/µL nuclease. Samples were subsequently lysed using EmulsiFlex cell disruptor by passing twice through it to maximise cell disintegration at 20,000-25,000 Bar. Afterwards 0.1% of polyethyleneimine was added. The resulting lysate was centrifuged at 30,000 *g* at 4°C for 30 minutes. The clarified lysate was filtered and loaded to HisTrap HP affinity column (GE Healthcare) followed by wash with excess of buffer and elution with buffer containing 500 mM imidazole. To biotinylate, pooled IMAC fractions containing protein were desalted to buffer 50 mM Tris/HCl pH 8.0 at 4°C, 150 mM NaCl, 1 mM DTT and incubated with BirA biotin ligase at ratio of 1:50 in a buffer supplemented with 5 mM $MgCl_2$, 211 µM biotin and 2.64 mM ATP at 4°C overnight. Finally,

the protein was subjected to size exclusion chromatography (SEC) using HiLoad 26/600 Superdex 75 pg (GE Healthcare) equilibrated in a buffer containing: 50 mM Tris/HCl pH 8.0 at 4°C, 300 mM NaCl, 1 mM DTT. Fractions containing protein were combined, aliquoted and flash frozen in liquid nitrogen. Samples were stored at -80 °C until further use. Crystallization and X-Ray structure determination.

Crystallization of GID4 protein was performed using the sitting drop vapour diffusion method. Protein was thawed and concentrated to ~4 mg/mL using Amicon Ultra-0.5 Centrifugal Filter Unit with 10 kDa molecular weight cut-off. To co-crystallize protein GID4 with ligands of choice, ligands were prepared in 100% DMSO as 20 mM stocks prior to incubation for 1 hour in ratio 1:20 (v/v; ligand to protein). Subsequently protein/ligand complexes were mixed 1:1 with precipitant solution (conditions either: 0.1 M HEPES pH 7.0-7.5, 0.1 M lithium sulfate, 10-25% PEG4000 or 0.1 M TRIS pH 8.0-8.5, 0.1 M lithium sulfate, 10-25% PEG4000 or 0.1 M Na HEPES pH 7.5; 2.5-10% 2-propanol and 6-20% PEG4000 or 0.1 M HEPES pH 7.0-7.5, 10-25% PEG3350 or 0.1 M TRIS pH 8.0-8.5, 10-25% PEG3350. Plates were incubated at 19°C and were inspected regularly. Crystals appeared within 24 hours in the form of thin needles. Prior to data collection, crystals were harvested in 30% glycerol prepared in GID4 precipitant solution and flash-cooled in liquid nitrogen. X-Ray diffraction data were recorded either at Deutsches Elektronen-Synchrotron DESY (Hamburg, Germany) or at Swiss Light Source (Villigen, Switzerland). Structural data were determined using the CCP4 suite of programs (Potterton et al. 2018). X-Ray data was first processed at beamline using XDS (Kabsch and Wolfgang 2010). The structures were solved using molecular replacement using PHASER (Mccoy et al. 2007) and Protein Data Bank (PDB) code 6CD9 or own structures as a search model. Refinement was carried out using REFMAC (Murshudov et al. 2011), with model building performed and compound descriptions generated using COOT (Emsley et al. 2010) and AceDRG (Long et al. 2017), respectively. Figures were prepared using PyMOL.

Differential scanning fluorimetry

The effect of the compounds on stabilization of the GID4 recombinant protein (amino acid region 116-300) was investigated with the Differential Scanning Fluorimetry (DSF) assay. First, the GID4 protein was thawed and centrifuged at 18000 rcf at 4°C for 5 min (Centrifuge 5430R, Eppendorf).

The protein concentration in the supernatant was measured (BioSpectrometer Basic, Eppendorf) and used to prepare a master mix containing 2.5 μM of GID4 in the assay buffer PBS, pH=7.4, 1 mM DTT. The master mix solution was pipetted into a 384-well PCR plate (4titude®, FrameStar®). The plates were spun down at 1000 rcf for 10 sec at room temperature (Centrifuge 5804R, Eppendorf). Subsequently, SYPRO™ Orange Protein Gel Stain (cat. nr S6650, Thermo Scientific) and tested compounds were added to the plate using Echo® 555 liquid handler (Labcyte Inc.). Fragments were tested at the c=500 μM and other compounds at c=100 μM in the final reaction mixture of V=10 μL per well. SYPRO™ Orange was used at the final dilution of 7.5x, and the DMSO content was adjusted to 2%. The plate was spun down at 1000 rcf at 22°C for 1 min (Centrifuge 5804R, Eppendorf), shaken by Vibroturbulator (Union Scientific) at level 10 for 1 min, spun down again, and incubated in the darkness for 15 min at room temperature. The readout was done using ViiA™ 7 Real-Time PCR System (Applied Biosystems) with a ramp rate of 0.1°C/s and the temperature range from 25°C to 95°C. The ΔTm and SSMD values (Zhang 2011) were determined by the dedicated in-house script.

Determinantion of KD^{GID4} by surface plasmon resonance

The molecular interactions were tested by surface plasmon resonance using Biacore 8K instrument (Cytiva). The immobilization was performed on the SA series S Biosensor chip (Cytiva) in all channels (ch1-8) based on a standard capture protocol with a flow rate of 10 μL/min. The surface of flow cell 2 was conditioned by three injections of regeneration solution (1M NaCl in 50mM NaOH). Subsequently, a solution of a biotinylated GID4 (amino acid region 116-300) at concentration of c=2.5 μg/ml in the immobilization buffer (PBS pH 7.4, 0.05% P-20, 1mM DTT) was injected over the sensor surface for 300 s. The immobilization levels were assessed and oscillated at about 2500 RU in each channel. Subsequently, both flow cells were blocked with 50 μM biotin-PEO3 (Biotium) for 90 s at 10 μL/min. All parts of the flow system except for the sensor chip were washed with 50% isopropanol in 1M NaCl and 50 mM NaOH. For the dose-response experiments, the stock solutions of 20 or 100 mM compounds were loaded onto a 384-well LDV plate (Labcyte Inc.). Compounds were transferred to the 384-well SPR destination plate (781280, Greiner) by the Echo® 555 liquid handler (Labcyte Inc.) to create 2-fold dilution dose-response curves. For fragments, the curves consisted of 6 points with concentrations ranging from c=31.25

to 1000 µM, and for other compounds, the curves consisted of 8 points with concentrations ranging from c=0.19 to 100 µM. Each well of the destination plate, containing 1010 nL of the compound backfilled with DMSO, was topped up with 99 µL of sample buffer (PBS pH 7.4, 0.05% P-20, 1 mM DTT, 1% DMSO) using a MultiFlo FX Dispenser (BioTek). The prepared plates were then centrifuged at 1000 rcf for 1 min at room temperature using the 5804R centrifuge (Eppendorf). A dedicated analysis method was configured in the Biacore 8K Control Software (Cytiva), which included an association time of t=60s, a dissociation time of t=120 s, and a flow rate of 30 µL/min. The method also incorporated positive, negative and a carry-over controls and solvent correction consisting of 8 points. The results were analyzed using the dedicated method in Biacore Insight Evaluation Software (Cytiva). In multi-cycle kinetics experiments, steady-state affinity for fragments was determined based on analyte binding early stability point (15 seconds from the beginning of injection), while for other compounds, it was determined based on analyte binding late stability point (5 seconds before the end of injection). In single-cycle kinetics experiments, the equilibrium dissociation constant was determined by using a 1:1 binding model.

Determinantion of KD^{BRD4} by surface plasmon resonance

The BRD4 was immobilized on a SA series S Biosensor chip (Cytiva). Firstly, the surface of flow cell 2 was conditioned by three injections of regeneration solution (1M NaCl in 50mM NaOH). Subsequently, the c=5 µg/ml solution of biotinylated BRD4 BD1 (amino acid region 44-168) in a running buffer (PBS pH 7.4, 0.05% P-20, 1mM DTT, 2% DMSO) was injected over the sensor surface for 300 s at a flow rate of 10 µL/min. The immobilization levels were assessed and oscillated at about 1400 RU in each channel. Subsequently, both flow cells were blocked with 50 µM biotin-PEO3 (Biotium) for 120 s at 30 µL/min. All parts of the flow system except for the sensor chip were washed with 50% isopropanol in 1M NaCl and 50 mM NaOH to remove nonspecifically bound biotin species from the microfluidics. Compounds were tested in the single-cycle kinetics mode using contact time 90 s, dissociation time 1800s and flow rate of 10 µL/min. The method contained startup, positive, negative and carry-over controls and solvent correction consisting of 4 points. Injections of running buffer (PBS pH 7.4, 0.05% P-20, 1mM DTT, 2% DMSO) were used as a reference. Compounds were injected at 9 concentrations per cycle in the range

from c=0.0015 to 10 µM (3-fold dilution). K_D^{BRD4} was determined in Biacore Insight Evaluation Software (Cytiva) by using 1:1 binding model.

Investigation of ternary complex formation by surface plasmon resonance

For investigation of ternary complex formation, the BRD4 protein was immobilized as described above. A dose-response experiment was then performed by using a single-cycle kinetics mode with the following parameters: contact time 90 s, dissociation time 1800s and flow rate 10 µL/min. The method contained solvent correction consisting of 4 points and a wash of the flow system with 50% DMSO to remove potential insolubilities. A reference cycle consisted of 9 injections of the untagged GID4 (amino acid region 116-300) in the range of concentrations of c=1.56-400 nM (2-fold dilution). The reference cycle was followed by the sample cycle where the same range of GID4 concentrations was mixed with the investigated compound in the 1:1 ratio. Each pair of the reference-sample cycles was separated by injection of running buffer serving as blank (PBS pH 7.4, 0.05% P-20, 1mM DTT, 2% DMSO). The data analysis was performed in Biacore Insight Evaluation Software (Cytiva). The sensorgrams from the sample cycle were blank- and reference-subtracted and fitted by using 1:1 binding model to determine the k_{off} and $K_D^{ternary}$. The half-life of the ternary complex was given by $t_{1/2} = 0.693/k_{off}$. Cooperativity factor α was calculated as $K_D^{BRD4}/K_D^{ternary}$.

Homogeneous Time Resolved Fluorescence

The effect of the bifunctional compounds on the mediation of a ternary complex between GID4 (amino acid region 116-300) and BRD4 (BD1) (amino acid region 44-168) was investigated using the Homogeneous Time-Resolved Fluorescence assay (HTRF). Firstly, protein solutions were centrifuged at 18000 rcf at 4°C for 5 min (Centrifuge 5430R, Eppendorf). The concentration of each protein was measured 3 times (BioSpectrometer Basic, Eppendorf) and the median of these measurements was used to prepare protein solutions. A mix of the GID4 and BRD4 proteins at the concentration of c=100 nM each, 52.8 nM acceptor mAb anti-6His-d2 (61HISDLA, Cisbio) and the 12 nM donor Eu cryptate-labeled streptavidin (610SAKLA, Cisbio) were prepared in PPI Europium detection buffer supplemented with 1 mM DTT. The prepared mix was dispensed at V=10 µl per

well on a 384-well low volume white microplate (Greiner, 784075). Subsequently, tested compounds were added to the plate in the range of concentrations from c=0.0097 to 20 µM (2-fold dilution, 12 points) by using Echo® 555 liquid handler (Labcyte Inc.). DMSO was backfilled to all wells, resulting in a final DMSO content of 0.5%. Wells containing only reaction mix and DMSO served as a background. The plate was sealed with a transparent film, and it was shaken by Vibroturbulator (Union Scientific) at level 3 for 30 sec at room temperature. Then, the plate was spun down at 1000 rcf for 60 sec at room temperature (Centrifuge 5804R, Eppendorf) to make sure the liquids were at the bottom of the wells. The plate was incubated at room temperature and the readout was performed after 60 min by using PHERAstar FSX Microplate Reader (BMG Labtech) in the time-resolved fluorescence dual emission mode (filters: TR 337 665 620). The data were analyzed using GraphPad Prism 9 and the dedicated script developed in-house to determine the EC_{50} values.

Chemical synthesis

General Methods. Solvents and reagents were of reagent grade and were used as supplied by the manufacturer. Organic extracts were routinely dried over anhydrous Na_2SO_4. Concentration refers to rotary evaporation under reduced pressure. Chromatography refers to flash chromatography using disposable Interchim PF-SiHP columns (4 to 120 g silica, 50 µm particle size) on a Interchim PuriFlash 5.020 or XS 520 Plus PuriFlash automatic purification system. Preparative HPLC was performed on a Waters AutoPurification system fitted with a YMC Triart C18 (250 x 20 mm, 5µ); alternatively Thermo Fisher Scientific Ultimate 3000 system fitted with Hypersil GOLD C18 (250 x 21.2 mm, 12µ) was used; the mobile phase consisted of a mixture of solvents: water (0.1% formic acid or 20 mmol/L NH_4HCO_3) and acetonitrile (w/wo 0.1% formic acid). Liquid chromatography-mass spectrometry (LC-MS) analyses were obtained with a Shimadzu model LCMS-2020 mass spectrometer utilizing ES-API ionization fitted with a phenomenex (Kinetex XB-C18, 2.6 µm particle size, 2.1*50 mm dimensions) reverse-phase column at 40 degrees Celsius. UPLC conditions: mobile phase A = 0.1% formic acid in water, mobile phase B = 0.1% formic acid in acetonitrile; flow rate = 0.5 mL/min; compounds were eluted with a gradient of 5% B/A to 95% B/A for 4 minutes. Alternatively, the LC-MS data were obtained with Water Acquity H Class UPLC attached with Waters SQD 2 mass spectrometer utilizing ES-API ionization fitted with a Waters

Acquity UPLC BEH C8 (2.1 x 50 mm, 1.7 μm particle size) reverse-phase column at 45 degrees Celsius. UPLC conditions: mobile phase A = 0.05% formic acid in water, mobile phase B = 0.05% formic acid in acetonitrile; flow rate = 0.8 mL/min; compounds were eluted with a gradient of 5% B/A to 95% B/A for 4 minutes. The purity of all the final compounds was shown to be >95% by UPLC–MS or UPLC. ^{1}H NMR spectra were obtained with a Bruker Advance 400 MHz or 500 MHz NMR instrument. Unless otherwise indicated, all protons were reported in Methanol-d4 or Dimethyl Sulfoxide-d6 solvent as parts per million (ppm) with respect to residual MeOD (3.31 ppm) or DMSO-d6 (2.50 ppm).

Cell culture

HEK293T cells (DSMZ, cat. ACC 635, RRID: CVCL_0045) were grown in DMEM high glucose with pyruvate (Gibco, cat. 11995065) supplemented with 10% fetal bovine serum (Gibco, cat. 10500-064), 1% Penicillin-Streptomycin (cat. L0022-100, Biowest).

Intracellular Target Engagement assay - GID4

The DNA fragment encoding full length human Glucose-induced degradation protein 4 homolog in fusion with N-terminal HiBiT tag was cloned into a piggyBac vector [HiBit-GID4(FL)] using HiFi DNA assembly reaction. Such created vector was used to transfect HEK293T cells. Stable expression in pools of cells was achieved using antibiotic selection (Puromycin, 2 μg/ml). Briefly, stably transfected cells, in serum-free cell culture medium (DMEM GlutaMAX), were seeded into 384-well PCR plates ($2x10^3$ cells / 10 μl / well) (Bio-Rad, HSP3865) using the multichannel Finnpipette (Thermo Fisher Scientific). Tested compounds (16 μM final tested concentration, 25 nl) or DMSO vehicle control (0.25 %) were subsequently added using Echo Acoustic Liquid Handler (E550, Labcyte) and incubated for 1h at 37 °C, 5% CO_2. The plate was sealed and heated at a temperature gradient (40.4 – 63.5°C) for 3.5 minutes using the pre-heated thermal cycler (C1000 Touch with 384-well module, Bio-Rad) and then cooled to 25 °C. PheraSTAR microplate reader (BMG Labtech) and Nano-Glo® HiBiT Lytic Detection system (10 μl, PROMEGA) were used for the signal readout (RLU values, Luminescence). T_{agg} for GID4 in the presence of DSMO was determined at 54.5 °C.

NanoBRET – in cell BRD4 Target Engagement Assay

Commercially available, HEK293 HiBiT-BRD4 cells stably expressing the LgBiT protein (HiBiT-BRD4 KI HEK293(LgBiT) CPM, cat. CS302312, Promega), and NanoBRET® Intracellular TE BET BRD Tracer (cat. N234A, Promega), were used. The assay was run in 384-well plate format (cat. 3574, Corning). Cells were prepared ($3.4x10^3$ cells/ml) in OptiMEM without phenol red (cat. 11058-021, Gibco) and they were mixed with the BET Tracer (0.1 mM stock or DMSO vehicle control). For the live mode assay, the Tracer (1 µl/well; final concentration 80 nM in 20 µl reaction) and 18.8 µl/well of cell suspension was used; for the lytic mode, except of the Tracer (1 µl/well, final concentration 30 nM in 20 µl reaction) and the cell suspension (16.8 µl/well), additionally 2 µl/well of digitonin was added. Next, the cell/Tracer mix (19.8 µl/well) was added onto the pre-plated tested compounds (100x concentrated, 0.2 µl/well; 11-point 2-fold dilution; Echo 555 acoustic dispenser, Labcyte). In the live mode assay, the plate was incubated at 37°C, 5% CO_2 for 2 hours, and then at room temperature for 15 minutes to cool down. In the lytic mode assay, there was no incubation. The complete NanoBRET reagent was prepared according to the manufacturer's recommendations, appropriately for live and lytic mode, and added to the tested wells (10 µl/well). The plate was incubated for 2 minutes at room temperature and the luminescence and fluorescence readings followed using CLARIOstar Multimode Plate Reader (donor emission RLU – 450nm; acceptor emission RFU – 610nm).

Protein structure analysis

A dataset of protein structures from the Protein Data Bank (17 structures) and our own structures (43 structures) were used. The structures were retrieved using the BioPython library (Cock et al. 2009). To ensure consistency, only structures with resolved residues 136, 137, 138, 163, 164, 165, 166, 167, 168, 169, 240, 241, 242, 243, 244, 245, 246, 250, 275, 276, 277, 278, 279 were retained. In cases where multiple chains were present, the first chain encountered was selected for further analysis. Four critical loops in the GID4 protein (L1 (136-138), L2 (163-169), L3 (240-250), and L4 (275-279)), previously described by (Dong et al. 2018), were used for detailed analysis. Further analysis was performed using a distance matrix based on the alpha carbon (CA) atoms. The distance matrix was standardized using a standard scaler, and PCA (Fabian Pedregosa et al. 2011) was applied to extract the principal components to explore the structural variability among the GID4 protein structures. From the PCA results, two key distances, d0 (T165-S250) and d1 (H244-E279), were extracted as representative measures of structural variability as the major components of PC0 and PC1. Subsequently, K-means clustering was used for clustering; the results were visualized using the seaborn and matplotlib libraries (Waskom et al. 2017; Hunter 2007). Visualization of the protein-ligand complexes was prepared by PyMol (*https://github.com/schrodinger/pymol-open-source*).

Calculation of PPI probability and pocket volume

We assessed the ligase's capability to form molecular glue-based ternary complexes using two predictors: pocket volume and PPI probability, predicted as surface patches with per-point PPI likelihoods. The probable PPI was predicted using the PESTO web tool (*https://pesto.epfl.ch/*) (Krapp et al. 2023) and saved as a PDB file.

Binding pocket parameters (volume, druggability, etc) were identified with the fpocket (Le Guilloux et al. 2009). The *vert.pqr files representing these pockets were converted into PDB format. Pocket definitions and known ligands were combined into a single PDB file.

To estimate the PPIs around the binding pocket, we considered only exposed residues. Solvent accessible surface area (calculated using the freeSASA tool (Mitternacht 2016) provided information about such exposed residues.

A custom Python script was employed to compute the mean PPI within a 9Å radius around the binding pocket, considering residues with an SASA value > 25Å² as exposed. The integrated data were plotted in PPI/volume coordinates.

ACCESSION CODES

All atomic coordinates and crystallographic results of GID4/small molecule complexes: GID4/1 (PDB: 9QDX), GID4/9 (PDB: 9QDY), GID4/14 (PDB: 9QDZ), GID4/18 (PDB: 9QZG), GID4/21 (PDB: 9QZI) and GID4/33 (PDB: 9QZH) were deposited to Protein Data Bank and are accessible from their websites (i.e. *https://www.rcsb.org/*).

ACKNOWLEDGEMENTS

The project nr POIR.01.01.01-00-0931/19 "Development of an integrated technology platform in the field of targeted protein degradation and its implementation to the pharmaceutical market" was co-financed by the European Regional Development Fund. The authors would like to acknowledge all members of the CT Team who contributed to this work. We would like to thank all the staff at: Deutsches Elektronen-Synchrotron DESY (Hamburg, Germany) and Swiss Light Source (Villigen, Switzerland) for their support during data collection. The authors would like to extend their gratitude to Donald Coppen for the meticulous proofreading and valuable suggestions.

Authors contributions:

Conceptualization of the manuscript and writing: DK, KD, MP, BW, DS, ZP; Review and edition of the manuscript: MB, TD, MJW; Chemistry conceptualization: SC, AM, ZP, BW, MJW; Chemical synthesis: AK, AM, WW; Protein purification: KP, MS, IHW, DG, KJ; Crystallography: MP, KG-M, MK, ANS, JW; Cell-based assays: EK, MC-B, TT; Modelling: DS; Biophysical assays: JA, SF, AP; Project coordination: IM, DK; Research supervised by: SC, MB, MJW

Competing interests

All authors are current or former employees of Captor Therapeutics S.A.

ABBREVIATIONS

TPD - targeted protein degradation

SBDD - Structure-based drug design

UPS - ubiquitin-proteasome system

CTLH - C-terminal to LisH complex

GID4 - Glucose-Induced Degradation protein 4 homolog

hGID4 - human GID4

HMGCS1 - 3-hydroxy-3-methylglutaryl (HMG)-coenzyme A (CoA) synthase 1

FBS - Fragment-Based Screening

DFS - Differential Scanning Fluorimetry

SPR - surface plasmon resonance

c – concentration

PDB - Protein Data Bank

PCA - principal component analysis

LMW - Low Molecular Weight

PPI - protein-protein interface

REFERENCES

Atilaw, Yoseph, Vasanthanathan Poongavanam, Caroline Svensson Nilsson, Duy Nguyen, Anja Giese, Daniel Meibom, Mate Erdelyi, and Jan Kihlberg. 2021. "Solution Conformations Shed Light on PROTAC Cell Permeability." ACS Medicinal Chemistry Letters 12 (1): 107–14. https://doi.org/10.1021/acsmedchemlett.0c00556.

Bagci, Halil, Martin Winkler, Federico Uliana, Jonathan Boulais, Weaam I Mohamed, Sophia L Park, Jean-François Côté, and Matthias Peter. 2023. "The hGID GID4 E3 Ubiquitin Ligase Complex Targets ARHGAP11A to Regulate Cell Migration." https://doi.org/10.1101/2023.07.20.549906.

Chana, Chetan K., Pierre Maisonneuve, Ganna Posternak, Nicolas G.A. Grinberg, Juline Poirson, Samara M. Ona, Derek F. Ceccarelli, et al. 2022. "Discovery and Structural

Characterization of Small Molecule Binders of the Human CTLH E3 Ligase Subunit GID4." Journal of Medicinal Chemistry 65 (19): 12725–46. https://doi.org/10.1021/acs.jmedchem.2c00509.

Chen, Shun Jia, Xia Wu, Brandon Wadas, Jang Hyun Oh, and Alexander Varshavsky. 2017. "An N-End Rule Pathway That Recognizes Proline and Destroys Gluconeogenic Enzymes." Science 355 (6323). https://doi.org/10.1126/SCIENCE.AAL3655.

Chrustowicz, Jakub, Dawafuti Sherpa, Joan Teyra, Mun Siong Loke, Grzegorz Popowicz, Jerome Basquin, Michael Sattler, J Rajan Prabu, Sachdev S Sidhu, and Brenda A Schulman. 2022. "Multifaceted N-Degron Recognition and Ubiquitylation by GID/CTLH E3 Ligases." https://doi.org/10.1101/2021.09.03.458554.

Cock, Peter J A, Tiago Antao, Jeffrey T Chang, Brad A Chapman, Cymon J Cox, Andrew Dalke, Iddo Friedberg, et al. 2009. "Biopython: Freely Available Python Tools for Computational Molecular Biology and Bioinformatics." Bioinformatics 25 (11): 1422–23. https://doi.org/10.1093/BIOINFORMATICS/BTP163.

Dalvie, Deepak K., Amit S. Kalgutkar, S. Cyrus Khojasteh-Bakht, R. Scott Obach, and John P. O'Donnell. 2002. "Biotransformation Reactions of Five-Membered Aromatic Heterocyclic Rings." Chemical Research in Toxicology. https://doi.org/10.1021/tx015574b.

Dong, Cheng, Shun-Jia Chen, Artem Melnykov, Sara Weirich, Kelly Sun, Albert Jeltsch, Alexander Varshavsky, Jinrong Min, and Edited F by Ulrich Hartl. 2020. "Recognition of Nonproline N-Terminal Residues by the Pro/N-Degron Pathway." https://doi.org/10.1073/pnas.2007085117/-/DCSupplemental.

Dong, Cheng, Heng Zhang, Li Li, Wolfram Tempel, Peter Loppnau, and Jinrong Min. 2018. "Molecular Basis of GID4-Mediated Recognition of Degrons for the Pro/N-End Rule Pathway Article." Nature Chemical Biology 14 (5): 466–73. https://doi.org/10.1038/s41589-018-0036-1.

Dunker, A Keith, Marc S Cortese, Pedro Romero, Lilia M Iakoucheva, and Vladimir N Uversky. 2005. "Flexible Nets The Roles of Intrinsic Disorder in Protein Interaction Networks." The FEBS Journal 272 (20): 5129–48. https://doi.org/10.1111/j.1742-4658.2005.04948.x

Emsley, P, B Lohkamp, W G Scott, and K Cowtan. 2010. "Features and Development of Coot." Urn:Issn:0907-4449 66 (4): 486–501. https://doi.org/10.1107/S0907444910007493.

Gottemukkala, Karthik V., Jakub Chrustowicz, Dawafuti Sherpa, Sara Sepic, Duc Tung Vu, Özge Karayel, Eleftheria C. Papadopoulou, et al. 2024. "Non-Canonical Substrate Recognition by

the Human WDR26-CTLH E3 Ligase Regulates Prodrug Metabolism." Molecular Cell 84 (10): 1948-1963.e11. https://doi.org/10.1016/j.molcel.2024.04.014.

Hämmerle, Marcus, Jürgen Bauer, Matthias Rose, Alexander Szallies, Michael Thumm, Stefanie Düsterhus, Dieter Mecke, Karl-Dieter Entian, and Dieter H Wolf. 1998. "Proteins of Newly Isolated Mutants and the Amino-Terminal Proline Are Essential for Ubiquitin-Proteasome-Catalyzed Catabolite Degradation of Fructose-1,6-Bisphosphatase of Saccharomyces Cerevisiae." http://www.jbc.org.

Hunter, John D. 2007. "Matplotlib: A 2D Graphics Environment." Computing in Science & Engineering 9 (3): 90–95. https://doi.org/10.1109/MCSE.2007.55.

Kabsch, Wolfgang. 2010. "XDS." Urn:Issn:0907-4449 66 (2): 125–32. https://doi.org/10.1107/S0907444909047337.

Kofink, Christiane, Nicole Trainor, Barbara Mair, Simon Wöhrle, Melanie Wurm, Nikolai Mischerikow, Michael Roy, et al. 2022. "A Selective and Orally Bioavailable VHL-Recruiting PROTAC Achieves SMARCA2 Degradation in Vivo."

Krapp, Lucien F, Luciano A Abriata, Fabio Cortés Rodriguez, and Matteo Dal Peraro. 2023. "PeSTo: Parameter-Free Geometric Deep Learning for Accurate Prediction of Protein Binding Interfaces." Nature Communications 2023 14:1 14 (1): 1–11. https://doi.org/10.1038/s41467-023-37701-8.

Le Guilloux, Vincent Le, Peter Schmidtke, and Pierre Tuffery. 2009. "Fpocket: An Open-Source Platform for Ligand Pocket Detection." BMC Bioinformatics 10 (1): 168. https://doi.org/10.1186/1471-2105-10-168.

Li, Yanran, Kaiwen Bao, Sun Jiyue, Ruixin Ge, Qiqing Zhang, Cheng Dong, et al. 2025. "Design of PROTACs utilizing the E3 ligase GID4 for targeted protein degradation". https://doi: 10.1038/s41594-025-01537-1.

Long, Fei, Robert A Nicholls, Paul Emsley, Saulius Gražulis, Andrius Merkys, Antanas Vaitkus, and Garib N Murshudov. 2017. "AceDRG: A Stereochemical Description Generator for Ligands." https://doi.org/10.1107/S2059798317000067.

Maple, Hannah J., Nat Clayden, Anne Baron, Callum Stacey, and Robert Felix. 2019. "Developing Degraders: Principles and Perspectives on Design and Chemical Space." MedChemComm 10 (10): 1755–64. https://doi.org/10.1039/c9md00272c.

Mccoy, Airlie J, Ralf W Grosse-Kunstleve, Paul D Adams, Martyn D Winn, Laurent C Storoni, and Randy J Read. 2007. "Phaser Crystallographic Software." J. Appl. Cryst 40:658–74. https://doi.org/10.1107/S0021889807021206.

Mitternacht, Simon. 2016. "FreeSASA: An Open-Source C Library for Solvent Accessible Surface Area Calculations." F1000Research 5. https://doi.org/10.12688/F1000RESEARCH.7931.1/DOI.

Murshudov, Garib N, Pavol Skubák, Andrey A Lebedev, Navraj S Pannu, Roberto A Steiner, Robert A Nicholls, Martyn D Winn, Fei Long, and Alexei A Vagin. 2011. "REFMAC5 for the Refinement of Macromolecular Crystal Structures." Urn:Issn:0907-4449 67 (4): 355–67. https://doi.org/10.1107/S0907444911001314.

Owens, Dominic D G, Matthew E R Maitland, Aliakbar Khalili Yazdi, Xiaosheng Song, Martin P Schwalm, Raquel A C Machado, Nicolas Bauer, et al. 2023. "A Chemical Probe to Modulate Human GID4 Pro/N-Degron Interactions." https://doi.org/10.1101/2023.01.17.524225.

Pedregosa, Fabian, Gaël Varoquaux, Alexandre Gramfort, Vincent Michel, Bertrand Thirion, Olivier Grisel, Mathieu Blondel, et al. 2011. "Scikit-Learn: Machine Learning in Python." Journal of Machine Learning Research 12 (85): 2825–30. http://jmlr.org/papers/v12/pedregosa11a.html.

Potterton, Liz, Jon Agirre, Charles Ballard, Kevin Cowtan, Eleanor Dodson, Phil R Evans, Huw T Jenkins, et al. 2018. "CCP4i2: The New Graphical User Interface to the CCP4 Program Suite." https://doi.org/10.1107/S2059798317016035.

Regelmann, Jochen, Thomas Schü Le, Frank S Josupeit, Jaroslav Horak, Matthias Rose, Karl-Dieter Entian, Michael Thumm, and Dieter H Wolf. 2003. "Catabolite Degradation of Fructose-1,6-Bisphosphatase in the Yeast Saccharomyces Cerevisiae: A Genome-Wide Screen Identifies Eight Novel GID Genes and Indicates the Existence of Two Degradation Pathways." Molecular Biology of the Cell 14:1652–63. https://doi.org/10.1091/mbc.E02-08.

Rui, Huan, Kate S. Ashton, Jaeki Min, Connie Wang, and Patrick Ryan Potts. 2023. "Protein-Protein Interfaces in Molecular Glue-Induced Ternary Complexes: Classification, Characterization, and Prediction." RSC Chemical Biology. Royal Society of Chemistry. https://doi.org/10.1039/d2cb00207h.

Santt, Olivier, Thorsten Pfirrmann, Bernhard Braun, Jeannette Juretschke, Philipp Kimmig, Hartmut Scheel, Kay Hofmann, Michael Thumm, and Dieter H Wolf. 2008. "The Yeast GID

Complex, a Novel Ubiquitin Ligase (E3) Involved in the Regulation of Carbohydrate Metabolism." Molecular Biology of the Cell 19:3323–33. https://doi.org/10.1091/mbc.E08.

Sundberg, Eric J, and Roy A Mariuzza. 2000. "Luxury Accommodations: The Expanding Role of Structural Plasticity in Protein–Protein Interactions." Structure 8 (7): R137–42. https://doi.org/10.1016/S0969-2126(00)00167-2.

Tutter, Antonin, Dennis Buckley, Andrei A Golosov, Xiaolei Ma, Wei Shu, Daniel J J Mckay, Veronique Darsigny, et al. 2025. "A Small Molecule VHL Molecular Glue Degrader for Cysteine Dioxygenase 1". Nat Chem Biol. doi: 10.1038/s41589-025-01936-x.

Waskom, Michael, Olga Botvinnik, Drew O'Kane, Paul Hobson, Saulius Lukauskas, David C Gemperline, Tom Augspurger, et al. 2017. "Mwaskom/Seaborn: V0.8.1 (September 2017)." Zenodo. https://doi.org/10.5281/zenodo.883859.

Watson, Edmond R, Scott Novick, Mary E Matyskiela, Philip P Chamberlain, Andres H de la Peña, Jinyi Zhu, Eileen Tran, Patrick R Griffin, Ingrid E Wertz, and Gabriel C Lander. 2022. "Molecular Glue CELMoD Compounds Are Regulators of Cereblon Conformation." Science 378 (6619): 549–53. https://doi.org/10.1126/science.add7574.

Yan, Jian, and Zhibing Zheng. 2023. "Discovery of Highly Potent CRBN Ligands and Insight into Their Binding Mode through Molecular Docking and Molecular Dynamics Simulations." ChemMedChem 18 (5): e202200573. https://doi.org/10.1002/CMDC.202200573.

Yazdi, Aliakbar Khalili, Sumera Perveen, Xiaosheng Song, Aiping Dong, Magdalena M Szewczyk, Matthew F Calabrese, Agustin Casimiro-Garcia, et al. 2023. "Chemical Tools for the Gid4 Subunit of the Human E3 Ligase C-Terminal to LisH (CTLH) Degradation Complex." https://doi.org/10.1101/2023.11.13.566858.

Yi, Sang Ah, Sara Sepic, Brenda A. Schulman, Alban Ordureau, and Heeseon An. 2024. "MTORC1-CTLH E3 Ligase Regulates the Degradation of HMG-CoA Synthase 1 through the Pro/N-Degron Pathway." Molecular Cell 84 (11): 2166-2184.e9. https://doi.org/10.1016/j.molcel.2024.04.026.

Zhang, Xiaohua Douglas. 2011. "Illustration of SSMD, z Score, SSMD*, Z* Score, and t Statistic for Hit Selection in RNAi High-Throughput Screens." Journal of Biomolecular Screening 16 (7): 775–85. https://doi.org/10.1177/1087057111405851.

ASSISTIVE WRITING TECHNOLOGIES

We used assistive writing technologies such as Grammarly and OpenAI's ChatGPT during manuscript preparation. These supplementary tools acted as editors, not as drivers of content creation. The listed authors thoroughly reviewed, revised, and selectively implemented suggested edits to ensure accuracy, consistency, and clarity. The responsibility for the paper's content and quality remains with the authors.